

## Mixing and ordering behavior in manganocolumbite-ferrocolumbite solid solution: A single-crystal X-ray diffraction study

SERENA C. TARANTINO\* AND MICHELE ZEMA

Dipartimento di Scienze della Terra, Università di Pavia, Via Ferrata 1, 27100 Pavia, Italy

### ABSTRACT

The structural changes upon cation substitution in natural  $AB_2O_6$  columbites have been studied by means of single-crystal X-ray diffraction. Most of the structural variations across the  $MnNb_2O_6$ - $FeNb_2O_6$  solid solution in completely ordered samples can be simply understood in terms of ionic radii. The substitution of Fe for the larger Mn cation causes a linear decrease of all unit-cell parameters. Going from manganocolumbite to ferrocolumbite the site A is reduced in volume and becomes less distorted. The oxygen cage around the cation assumes a more regular arrangement since the mismatch between A and B chains decreases. At the same time, the divalent cation moves toward the barycenter of the polyhedron. The B site, which is not involved in the Fe-Mn cation substitution, maintains its geometry unchanged. Ordering of divalent cations at A sites and pentavalent cations at B sites causes linear variations of  $a$  and  $c$  cell parameters. A non-linear behavior is shown by the  $b$  cell parameter that shows a minimum at order parameter  $Q_m \sim 0.7$ . A discontinuity at this  $Q_m$  value is also shown by other structural parameters. Cation ordering also causes volume variations of the two octahedral sites as a consequence of the different ionic radii of the various species. Octahedral bond-length distortion parameters show that the B site is in general more distorted than the A site; distortion of the B site increases with ordering due to higher cation-cation repulsion along the B octahedral chain and to the second-order Jahn-Teller (SOJT) effect. Octahedral chains respond to modifications of the polyhedra by folding along the common edge.

### INTRODUCTION

Columbite-tantalite minerals are the predominant Nb-Ta phases found in granitites<sup>†</sup>). Although the 3d transition metals mainly occupy the A site, a considerable degree of cation disorder can occur between the A and B sites. The different cation occupancy of the sites leads to changes in the unit-cell dimensions and to distortions of the oxygen octahedra. In the disordered structure, the cations are randomly distributed, resulting in a unit cell with an  $a$  dimension of approximately 4.8 Å and space group  $Pbcn$ . Ordering of Fe + Mn (ionic radii 0.78 Å and 0.83 Å, respectively, according to Shannon 1976) at A sites and Nb + Ta (i.e., 0.64 Å for both pentavalent cations) at B sites results in an ...*ABBABB*... site population sequence on (100) and a consequent tripling of the  $a$  repeat to approximately 14.2 Å. The  $Pbcn$  symmetry is maintained. The complete ordered structural state corresponds to the thermodynamically stable phase as determined by Giese (1975) on the basis of electrostatic energy calculations, and may be obtained by thermal treatment of natural samples (Nickel et al. 1963; Ercit et al. 1995).

Nature provides samples with a large compositional variation and structural states ranging from highly disordered to completely ordered. As yet, there have been no systematic studies of the structural mechanism by which variations in cation size and charge are accommodated. Structural information on synthetic ordered end-members  $FeNb_2O_6$ ,  $MnNb_2O_6$ , and  $MnTa_2O_6$  were

given by Weitzel (1976) from neutron-diffraction powder patterns. X-ray single-crystal structure refinements were carried out by Grice et al. (1976) using data from heat-treated natural manganotantalite. The order-disorder process also remains poorly understood. It has been suggested (Černý et al. 1986) that columbite-group minerals crystallize initially in the disordered state, and that further ordering is related to the cooling rate of their host igneous bodies. Cation ordering in natural columbites gives rise to changes in unit-cell dimensions. The relationships between unit-cell parameters and degree of order in the minerals of the columbite group have been studied by several authors (Nickel et al. 1963; Turnock 1966; Komkov 1970; Černý and Turnock 1971; Wise et al. 1985; Černý et al. 1986). On the basis of these data, Ercit et al. (1995) derived the following equation to obtain the degree of order:

$$Q\% (\pm 5\%) = 1727 - 941.6 (c - 0.2329 a) \quad (1)$$

The presence of strong X-ray absorbers such as Ta and Nb in the columbite crystal structure limits the possibility of determining with ease the degree of order from site occupancies obtained by single-crystal X-ray diffraction. Determination of cation distribution in two natural partially ordered columbites from X-ray single-crystal structure refinements was attempted by Wenger et al. (1991). The degrees of order calculated from site occupancies were indeed similar to those obtained using Equation 1 but, as the authors stated, these values did not necessarily reflect the true cation distributions, being a function of a given

\* E-mail: tarantino@crystal.unipv.it

refinement model in which many structural constraints were assumed. Experimental determinations of the degree of order in natural columbites were also obtained by Augsburg et al. (1999) by means of Mössbauer spectroscopy data, and they are too in good agreement with the Equation 1.

The aim of this study was to fully characterize the mechanism of formation of solid solution and cation-ordering behavior in the system  $\text{MnNb}_2\text{O}_6\text{-FeNb}_2\text{O}_6$ . Four ordered natural samples with composition across the  $\text{MnNb}_2\text{O}_6\text{-FeNb}_2\text{O}_6$  join were examined. Cation ordering has been characterized in two natural columbite crystals with compositions close to those of the end-members, hence focusing attention on the divalent-Nb<sup>5+</sup> exchange. Different structural states corresponding to different degrees of order, induced by thermal treatments in the temperature range 500–950 °C, were obtained by quenching experiments. Single-crystal X-ray diffraction (SC-XRD) was used to characterize the structural variations as a function of iron content and ordering degree. The degrees of order were calculated on the basis of site occupancies obtained by X-ray structure refinements.

This represents the first work in which the evolution of the degree of order in columbite crystals has been systematically determined by means of X-ray structure refinements. Different strategies of data collection were also compared, particularly with respect to absorption correction methods.

## EXPERIMENTAL METHODS

### Samples

For this study four natural columbite samples showing similar  $X_{\text{Nb}}$  [ $X_{\text{Nb}} = \text{Nb}/(\text{Nb} + \text{Ta}) - 0.95$ ] and covering a wide range of  $X_{\text{Fe}}$  [ $X_{\text{Fe}} = \text{Fe}/(\text{Fe} + \text{Mn})$ ] were chosen. A list of the samples investigated is given in Table 1. Small fragments of each sample were annealed in sealed evacuated silica tubes at 950 °C for 115 h to induce cation ordering (Nickel et al. 1963; Ercit et al. 1995). The fragments were then crushed for selection of single-crystals suitable for SC-XRD analysis.

Samples BRA and KRA were also used to characterize the ordering process. X-ray diffraction analyses were carried out using one crystal from each sample. After the preliminary SC-XRD study, in which the initial ordering state was determined, the two selected crystals were submitted to subsequent *ex situ* annealing experiments in order to reach different ordering states. Annealing experiments were performed in sealed evacuated quartz vials held in a vertical furnace. At the end of each annealing experiment the crystals were quenched and a new SC-XRD analysis was performed to determine the degree of order and calculate all the relevant geometrical parameters.

### Electron microprobe analyses

Chemical analyses of the same single-crystals used for the X-ray diffraction experiments were done at the Department of Earth Sciences of the University of Modena with an ARL-SEM-Q electron microprobe operating in the wavelength dispersive (WDS) mode. Crystal KRA n.3p was lost during polishing, hence chemical analysis was performed on different fragments of the rock sample. Operating conditions were 15 kV and 20 nA sample current. Counting times were 20 s for peaks and 5 s for backgrounds. The standards used were: Nb metal (NbL $\alpha$ ), Ta metal (TaM $\alpha$ ), ilmenite (FeK $\alpha$ , TiK $\alpha$ ), Sc metal (ScK $\alpha$ ), spessartine (MnK $\alpha$ ), cassiterite (SnL $\alpha$ ), anorthite (CaK $\alpha$ ), and W metal (WM $\alpha$ ). X-ray counts were converted into oxide weight percentages using the PROBS correction program

**TABLE 1.** Details of natural columbite samples studied

Sample	Location	Museum no.
Col BRA*	S. José de Safira, Minas Gerais, Brazil	41248
Col AMB*	Ambatofotsikely, Madagascar	5594
Col RIO*	Rio Arriba Co., Globe Mine, U.S.A.	46713
Col KRA†	Kragero, Norway	4814

\* Provided by Museo di Storia Naturale - Sezione di Mineralogia of the University of Florence.

† Provided by Museo di Mineralogia of the University of Pavia.

(Donovan and Rivers 1990). The analyses are precise to within 1% for major elements and 3–5% for minor elements. Only the spot analyses which satisfied the following conditions were averaged: (1) total oxide amount =  $100 \pm 1.5$ ; (2) total cation content =  $3.000 \pm 0.01$  atoms on the basis of six oxygen atoms. The analyses and the formulae calculated on the basis of six oxygen atoms for the columbite samples are given in Table 2.

### X-ray single-crystal diffraction

Two different strategies of data collection were used. A Bruker AXS Smart Apex three-circle diffractometer equipped with a CCD detector was used for all ordered crystals and for sample BRA n.18, while a conventional Philips PW1100 four-circle diffractometer was used for sample KRA n.4.

**X-ray data collection: CCD detector.** Data collections were carried out at 50 kV and 30 mA with graphite-monochromatized MoK $\alpha$  radiation ( $\lambda = 0.71073$  Å). The Bruker SMART system of programs was used for preliminary crystal lattice determination and X-ray data collection. For each crystal, a total of 5400 frames (resolution:  $512 \times 512$  pixels) were collected with six different goniometer settings using the  $\omega$ -scan mode (scan width:  $0.2^\circ \omega$ ; exposure time: 5 s/frame; detector-sample distance: 5 cm). Completeness of measured data was achieved up to  $35.1^\circ \theta$ . The Bruker SAINT+ program was used for data reduction, including intensity integration, background, and Lorentz-polarization corrections. Final unit-cell parameters were obtained by the Bruker GLOBAL least-squares orientation matrix refinement procedure, based on the positions of all measured reflections, and are reported in Table 3. The semi-empirical absorption correction of Blessing (1995), based on the determination of transmission factors for equivalent reflections, was applied using the Bruker program SADABS. Details for data collections are reported in Table 3.

**X-ray data collection: conventional techniques.** Intensity data were collected at 55 kV and 30 mA using graphite-monochromatized MoK $\alpha$  radiation ( $\lambda = 0.71073$  Å). Horizontal and vertical apertures were  $2.0^\circ$  and  $1.5^\circ$ , respectively. The equivalent reflections  $hkl$  and  $\bar{h}\bar{k}l$  were measured in the  $2\text{--}35^\circ \theta$  range using the  $2\theta$ -scan mode. Three standard reflections were collected every 200 reflections. The net X-ray diffraction intensities were obtained by measuring step-scan profiles and analyzing them with the Lehman and Larsen (1974)  $\sigma/I$  method, as modified by Blessing et al. (1974). Unit-cell parameters were derived from a least-squares procedure, based on a locally improved version (Cannillo et al. 1983) of the Philips LAT routine, taking into account 50 to 60  $d$ -spacings measured considering all the reflections in the range  $3^\circ < \theta < 25^\circ$ . Intensities were corrected for Lorentz and polarization effects, and a semi-empirical absorption correction was applied using the  $\psi$ -scan method of North et al. (1968). Unit-cell parameters and relevant parameters on data collections performed by means of the conventional diffractometer on sample KRA n.4 are reported in Table 3.

By comparing data from samples BRA n.18 and KRA n.4 reported in Table 3, it is clear that better-quality X-ray data were obtained from the CCD diffractometer. This is at least in part due to the different methods adopted for absorption correction. Absorption is very strong in these samples due to the presence of heavy elements such as Ta and Nb. Transmission factor ratios  $T_{\text{min}}/T_{\text{max}}$  ranged between 0.47 and 0.35. The  $\psi$ -scan method can depend strongly on the reflections chosen and intensity variations about the diffraction vector can result from anisotropic primary or secondary extinction rather than absorption. The multiscan method of Blessing (1995), made possible by the extensive set of equivalent reflections collected by the CCD diffractometer, seems much more appropriate and effective.

**Structure refinements.** The values of equivalent reflections were averaged and the resulting discrepancy factors are reported in Table 3 for completely ordered samples and for crystals BRA n.18 and KRA n.4. The structure refinements were carried out in space group *Pben* using the program Crystals (Betteridge et al. 2003). For the ordered samples, the divalent cation ( $\text{Fe}^{2+}$  for samples BRA and AMB;  $\text{Mn}^{2+}$  for samples RIO and KRA) was considered fully ordered at the A site while pentavalent cations were assumed to occupy the B site. For samples KRA and BRA at the various degrees of order, the divalent cation ( $\text{Fe}^{2+}$  for sample BRA;  $\text{Mn}^{2+}$  for sample KRA) and the two pentavalent cations were allowed to partition between the two octahedral A and B sites. The overall Nb/Ta ratio was constrained on the basis of the electron microprobe analyses. Moreover, for sample KRA, the small amounts of impurities were partitioned as follows: Ca was considered fully ordered at the A site while Ti was equally distributed among the sites and not refined.

The atomic scattering curves were taken from the *International Tables for X-ray Crystallography* (Ibers and Hamilton 1974). Structure factors were weighted according to Chebichev schemes (Carruthers and Watkin 1979). An isotropic extinction parameter  $x$  (Larson 1970) was refined. In addition to  $x$  and the scale factor, 13 atomic positions, anisotropic displacement parameters, and site occupancies

TABLE 2. Electron microprobe analyses

	Col BRA n.3	Col BRA n.18	Col AMB n.3	Col RIO n.5	Col KRA n.4	Col KRA
<b>Oxide (wt%)</b>						
MnO	4.17(6)	4.30(4)	9.63(38)	10.92(60)	16.44(18)	16.31(12)
FeO	16.09(13)	16.46(12)	10.06(40)	9.47(67)	2.96(7)	3.03(25)
TiO <sub>2</sub>	0.74(1)	0.68(6)	2.75(12)	1.48(30)	1.59(7)	1.78(5)
Sc <sub>2</sub> O <sub>3</sub>	0.02(1)	0.04(1)	0.91(3)	–	0.04(3)	0.03(1)
CaO	0.02(1)	0.02(1)	0.01(1)	0.02(1)	0.17(5)	0.13(1)
SnO <sub>2</sub>	0.02(2)	0.03(2)	0.17(5)	0.01(1)	0.15(3)	0.12(1)
Ta <sub>2</sub> O <sub>5</sub>	5.51(29)	5.96(32)	5.66(28)	5.96(41)	11.24(21)	9.52(87)
WO <sub>3</sub>	0.20(12)	0.16(8)	0.14(8)	0.96(16)	0.04(7)	0.02(2)
Nb <sub>2</sub> O <sub>5</sub>	73.56(71)	72.80(42)	70.82(99)	70.53(83)	67.29(83)	68.15(39)
Sum	100.33(80)	100.45(42)	100.17(76)	99.34(77)	99.92(74)	99.10(68)
<b>Atoms per formula unit (based on six oxygen atoms)</b>						
Mn	0.202(4)	0.208(2)	0.462(16)	0.534(33)	0.812(11)	0.806(3)
Fe	0.767(8)	0.787(7)	0.476(21)	0.457(30)	0.145(4)	0.148(13)
Ti	0.032(1)	0.029(3)	0.117(5)	0.064(12)	0.070(3)	0.078(2)
Sc	0.001(1)	0.002(1)	0.045(2)	–	0.002(1)	0.001(1)
Ca	0.001(1)	0.002(1)	0.001(1)	0.001(1)	0.010(3)	0.008(1)
Sn	0.001(1)	0.001(1)	0.004(1)	0.001(1)	0.004(1)	0.003(1)
Ta	0.085(4)	0.093(5)	0.087(5)	0.094(7)	0.178(3)	0.151(14)
W	0.003(2)	0.002(1)	0.002(1)	0.014(2)	0.001(1)	0.001(1)
Nb	1.897(4)	1.881(5)	1.811(11)	1.841(6)	1.774(9)	1.789(9)
Sum	2.988(7)	3.004(5)	3.005(6)	3.005(7)	2.996(9)	2.994(8)
X <sub>Fe</sub>	0.792	0.791	0.507	0.461	0.152	0.155
X <sub>Nb</sub>	0.957	0.953	0.954	0.951	0.909	0.922
<b>Expected unit-cell parameters for corresponding ordered columbites*</b>						
a (Å)	14.2910	14.2914	14.3352	14.3440	14.3955	14.3913
b (Å)	5.7354	5.7355	5.7430	5.7449	5.7545	5.7541
c (Å)	5.0567	5.0568	5.0658	5.0676	5.0782	5.0779

Notes: Standard deviations are given in parentheses.  $X_{Fe} = Fe / (Fe + Mn)$ ;  $X_{Nb} = Nb / (Nb + Ta)$ .

\* Theoretical values are calculated using Equations 3, 4, and 5 in Ercit et al. (1995).

TABLE 3. Unit-cell parameters and details for data collections and structure refinements

	a (Å)	b (Å)	c (Å)	V (Å <sup>3</sup> )	Q	I <sub>tot</sub>	I <sub>ind</sub>	R <sub>int</sub> (%)	R <sub>all</sub> (%)	wR <sub>all</sub> (%)	S	m.a.n. A site	m.a.n. B site	m.a.n. A+2B	
<b>Ordered samples</b>															
BRA n.3	14.2877(10)	5.7363(4)	5.0561(3)	414.39	1	6658	956	2.3	2.23	3.69	1.240	26	43.14	112.28	
AMB n.3	14.3267(12)	5.7392(5)	5.0674(4)	416.66	1	6886	965	1.8	2.41	3.32	1.105	26	42.57	111.14	
RIO n.5	14.3434(12)	5.7415(5)	5.0665(4)	417.24	1	6700	949	1.8	3.48	6.19	0.941	25	42.12	109.24	
KRA n.3p	14.4003(12)	5.7501(5)	5.0784(4)	420.51	1	6916	972	1.9	3.01	5.17	0.922	25	43.34	111.68	
<b>BRA n.18</b>															
Untreated	14.2427(3)	5.7290(1)	5.0856(1)	414.97(1)	0.62	6713	950	2.2	2.62	4.89	0.948	29.99	40.63	111.25	
600 °C 20m	14.2445(3)	5.7265(1)	5.0789(1)	414.29(1)	0.69	6689	948	1.9	2.38	4.63	0.987	29.25	40.99	111.23	
650 °C 20m	14.2501(3)	5.7263(1)	5.0767(1)	414.26(1)	0.72	6708	949	2.0	2.41	4.88	0.981	28.96	41.14	111.25	
650 °C 200m	14.2582(3)	5.7290(1)	5.0748(1)	414.53(1)	0.75	6687	948	2.1	2.15	4.20	0.995	28.61	41.29	111.20	
700 °C 5m	14.2600(3)	5.7293(1)	5.0746(1)	414.59(1)	0.76	6621	952	2.0	2.42	4.80	1.024	28.51	41.40	111.30	
700 °C 20m	14.2658(3)	5.7299(1)	5.0748(1)	414.82(1)	0.77	6689	955	1.9	2.21	4.42	1.026	28.42	41.40	111.22	
800 °C 7m	14.2733(3)	5.7317(1)	5.0646(1)	414.34(1)	0.88	6619	942	2.1	2.23	4.64	1.066	27.02	42.09	111.20	
800 °C 40m	14.2744(3)	5.7321(1)	5.0616(1)	414.15(1)	0.91	6804	954	2.1	2.27	4.12	0.977	26.99	42.11	111.20	
950 °C 3h	14.2852(3)	5.7361(1)	5.0574(1)	414.41(1)	0.98	6853	969	2.5	2.38	4.49	0.957	26.12	42.57	111.26	
<b>KRA n.4</b>															
Untreated	14.325(8)	5.744(3)	5.113(3)	420.7(4)	0.54	3969	915	3.3	4.59	4.69	0.926	31.53	40.54	112.62	
500 °C 15h	14.344(10)	5.739(1)	5.105(3)	420.2(5)	0.66	3957	912	3.3	3.75	4.81	0.999	30.30	41.18	112.64	
530 °C 92h	14.334(7)	5.737(4)	5.096(5)	419.1(5)	0.72	2128	911	3.1	4.04	5.21	1.080	29.78	41.43	112.64	
600 °C 67h	14.352(8)	5.740(4)	5.093(5)	419.5(5)	0.79	2181	929	2.0	3.88	4.91	1.090	28.85	41.89	112.64	
600 °C 177h	14.352(7)	5.740(3)	5.090(4)	419.3(5)	0.82	1862	845	3.0	3.90	5.10	1.043	28.58	41.99	112.57	
700 °C 20m	14.380(9)	5.745(3)	5.088(3)	420.4(4)	0.90	2180	928	3.1	4.04	5.13	1.159	27.50	42.56	112.62	
800 °C 15m	14.380(10)	5.750(4)	5.084(4)	420.5(5)	0.94	2182	929	2.0	3.50	4.66	1.036	27.01	42.83	112.68	
800 °C 24h	14.395(8)	5.753(3)	5.083(6)	421.0(6)	0.97	2187	931	2.2	3.26	5.08	1.099	25.84	43.46	112.76	

Notes: standard deviations are given in parentheses. Q is the degree of cation ordering calculated as  $Q = [1727 - 941.6(c - 0.2329a)]/100$  (Ercit et al. 1995). For the ordered samples the A site was considered fully occupied by the most abundant divalent cation.  $R_{int} = \sum |F_o^2 - F_c^2(\text{mean})| / \sum [F_o^2]$ ;  $R_{all} = \sum |F_o - |F_c|| / \sum [F_o]$ ;  $S = [\sum [w(F_o^2 - F_c^2)^2] / (n - p)]^{0.5}$ , where n is the number of reflections and p is the total number of parameters refined. I<sub>tot</sub> is the total number of reflections after merging identical reflections (redundancy of measurements was ca. 1.75); I<sub>ind</sub> is the number of independent reflections used for structure refinements. m.a.n. is the mean atomic number.

were refined simultaneously. No correlation greater than 0.81 was observed. Final discrepancy factors, together with the goodness of fit S and the number of total and unique reflections I<sub>tot</sub> and I<sub>ind</sub>, are reported in Table 3 for all of the samples.

The divalent cation (Fe<sup>2+</sup> for sample BRA n.18 and Mn<sup>2+</sup> for sample KRA n.4) and the two pentavalent cations were refined independently at both octahedral sites.

The order parameter used here to describe the degree of (Mn,Fe)/(Nb,Ta) order between A and B sites is taken as  $Q_m = |X_{Fe+Mn(A)} - X_{Fe+Mn(B)}| = |X_{Nb+Ta(B)} - X_{Nb+Ta(A)}|$ , where  $X_{Fe+Mn(A)}$  and  $X_{Fe+Mn(B)}$  represent the sum of molar fractions of Fe<sup>2+</sup> and Mn<sup>2+</sup>

occupying the A and B sites, respectively, and similarly for  $X_{Nb+Ta(B)}$  and  $X_{Nb+Ta(A)}$ .  $Q_m$  values determined for crystals KRA n.4 and BRA n.18 are reported in Table 4 and are in good agreement with those calculated from the unit-cell parameters using Equation 1.

Analysis of site occupancies (see data in Table 4) as a function of  $Q_m$  seems to indicate that the Nb/Ta ratio may not be constant within the sites. This is particularly evident in sample KRA n.4, which shows a slightly higher Ta content. If this is correct, different ordering rates for the two pentavalent cations should be considered. Further studies are in hand using more suitable columbite samples

with Nb/Ta close to 0.5.

Bond distances and other geometrical parameters are given in Table 5 for ordered samples, and in Tables 6a and 6b for crystals BRA n.18 and KRA n.4, respectively.

## RESULTS AND DISCUSSION

The structure of columbite is a derivative of the  $\alpha$ - $\text{PbO}_2$  structure type in which the oxygen atoms assume a distorted HCP configuration and the cations occupy one-half of the available octahedral interstices. The resulting symmetry is orthorhombic (space group  $Pbcn$ ), and there are two distinct octahedral sites ( $4c$  and  $8d$ ). Typical bond lengths are 2.10–2.20 Å for the A site and 1.80–2.27 Å for the B site. The crystal structure of columbite is depicted in Figure 1. The fundamental building units are zigzag chains of edge-sharing octahedra that run parallel to the  $c$  axis. Individual chains are connected by corner-sharing to form a three dimensional framework. In this way modifications of each octahedron result in deformation of the neighboring octahedral chains through the sharing of oxygen atoms. In fact, the A and B chains respond to the reciprocal changes of the octahedra by folding along the common edge, which is a low-energy deformation.

In the following discussion, octahedral distortions were analyzed with the ELD parameter, which measures deviation of edge

**TABLE 4.** Site occupancies and  $Q_m$  for crystals BRA n.18 and KRA n.4

	Site A			Site B			$Q_m$
	$M^{2+}$	$Nb^{5+}$	$Ta^{5+}$	$M^{2+}$	$Nb^{5+}$	$Ta^{5+}$	
<b>BRA n.18</b>							
Untreated	0.745(4)	0.250(4)	0.005	0.127(2)	0.825(2)	0.048(1)	0.618
600 °C 20m	0.790(4)	0.207(4)	0.003	0.105(2)	0.846(2)	0.049(1)	0.685
650 °C 20m	0.809(4)	0.188(4)	0.003	0.095(2)	0.856(2)	0.049(1)	0.714
650 °C 200m	0.830(3)	0.168(3)	0.002	0.085(2)	0.866(2)	0.049(1)	0.745
700 °C 5m	0.835(4)	0.164(4)	0.001	0.083(2)	0.868(2)	0.050(1)	0.752
700 °C 20m	0.839(3)	0.161(3)	0.000	0.080(2)	0.870(2)	0.050(1)	0.759
800 °C 7m	0.932(3)	0.068(3)	0.000	0.034(2)	0.916(2)	0.050(1)	0.898
800 °C 40m	0.934(4)	0.066(4)	0.000	0.033(2)	0.917(2)	0.050(1)	0.902
950 °C 3h	0.992(4)	0.008(4)	0.000	0.004(2)	0.945(2)	0.051(1)	0.988
<b>KRA n.4</b>							
Untreated	0.685(2)	0.235(3)	0.046	0.140(1)	0.770(1)	0.066(4)	0.565
500 °C 15h	0.756(7)	0.167(7)	0.042	0.105(4)	0.804(6)	0.068(4)	0.674
530 °C 92h	0.800(2)	0.123(2)	0.044	0.083(2)	0.826(2)	0.067(2)	0.742
600 °C 67h	0.848(1)	0.077(2)	0.040	0.059(2)	0.849(1)	0.069(2)	0.817
600 °C 177h	0.866(1)	0.061(3)	0.039	0.050(2)	0.857(2)	0.069(2)	0.844
700 °C 20m	0.915(3)	0.023(3)	0.028	0.025(4)	0.876(3)	0.075(2)	0.922
800 °C 15m	0.940(1)	0.004(2)	0.023	0.013(3)	0.885(2)	0.078(1)	0.960
800 °C 24h	0.966	0	0	0	0.889(1)	0.089(1)	1

Note: Standard deviations are given in parentheses.

lengths from a regular octahedron, as proposed by Renner and Lehmann (1986), and the offset of the central metal atom from the geometrical centre (Ct) of the polyhedron, which in turn gives an indication of the distortion of the bond lengths. These values are reported in Tables 5, 6a, and 6b together with the octahedral angle variance (OAV) and octahedral quadratic elongation (OQE) parameters (Robinson et al. 1971). Interpolyhedral connections were analyzed by evaluating the angles between two edge-shar-

**TABLE 5.** Bond distances (Å) and selected geometrical parameters for ordered columbite samples

	BRA n.3	AMB n.3	RIO n.5	KRA n.3p
<b>Site A</b>				
A-O1 (x2)	2.1063(11)	2.1144(11)	2.1187(25)	2.1347(19)
A-O2 (x2)	2.1315(11)	2.1381(12)	2.1387(27)	2.1572(19)
A-O2 (x2)	2.1588(11)	2.1799(12)	2.1873(26)	2.2206(20)
Average	2.1322	2.1441	2.1482	2.1708
Volume (Å <sup>3</sup> )	12.645	12.807	12.873	13.227
OQE	1.015	1.018	1.018	1.021
OAV	51.31	60.63	61.69	71.56
ELD	4.66	4.95	5.04	5.20
Ct(A)-A	0.2202(4)	0.2421(4)	0.2450(8)	0.2686(6)
<b>Site B</b>				
B-O1	1.9199(11)	1.9213(11)	1.9234(25)	1.9224(19)
B-O1	2.0761(10)	2.0759(11)	2.0719(24)	2.0678(19)
B-O2	1.8011(10)	1.8040(11)	1.8034(25)	1.7951(19)
B-O3	2.0651(11)	2.0657(11)	2.0630(25)	2.0644(18)
B-O3	1.9575(10)	1.9571(11)	1.9578(24)	1.9516(18)
B-O3	2.2746(10)	2.2691(11)	2.2759(24)	2.2857(18)
Average	2.0157	2.0155	2.0159	2.0145
Volume (Å <sup>3</sup> )	10.495	10.501	10.502	10.480
OQE	1.032	1.032	1.032	1.033
OAV	92.36	90.21	91.29	91.25
ELD	3.44	3.52	3.60	3.57
Ct(B)-B	0.3303(2)	0.3249(2)	0.3270(3)	0.3285(2)
<b>Interpolyhedral geometrical parameters</b>				
A-A	3.1975(4)	3.2311(4)	3.2381(7)	3.2786(6)
B-B	3.2662(2)	3.2668(2)	3.2689(4)	3.2740(3)
Ct(A)-Ct(A)	2.9485	2.9551	2.9578	2.9680
Ct(B)-Ct(B)	2.9156	2.9208	2.9207	2.9246
Tilt A (°)	68.13	67.59	67.61	66.83
Tilt B <sub>A</sub> (°)	77.44	78.08	78.33	79.43
Tilt B <sub>B</sub> (°)	54.16	53.06	52.84	51.48

Note: standard deviations are given in parentheses.

ELD (Edge Length Distortion) is defined as

$$ELD = \frac{100}{n} \sum_{i=1}^n \frac{(X - X)_i - (X - X)_m}{(X - X)_m} \%$$

where  $m$  = average (Renner and Lehmann 1986). Ct(A) and Ct(B) are the centroids of polyhedra A and B, respectively.

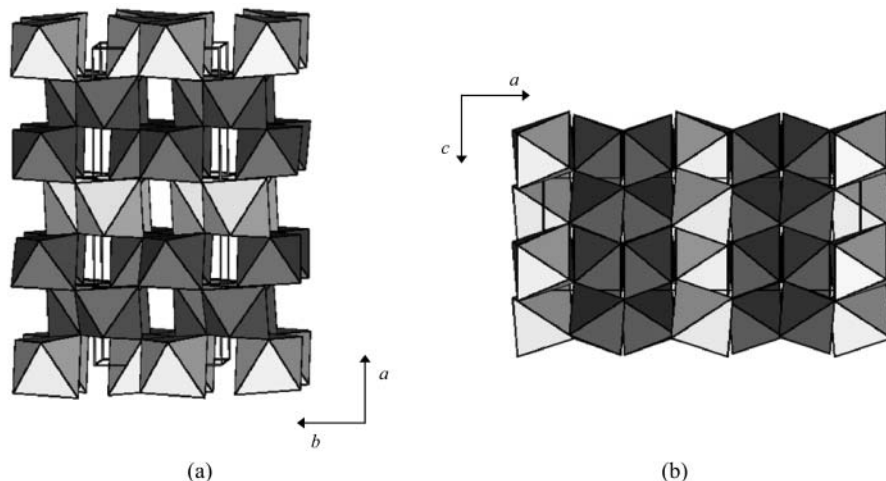


**FIGURE 1.** The crystal structure of columbite viewed (a) along [001] and (b) [010].

**TABLE 6A.** Bond distances (Å) and selected geometrical parameters for sample BRA n.18

$Q_m$	0.618	0.685	0.714	0.745	0.752	0.759	0.898	0.902	0.988
<b>Site A</b>									
A-O1 (x2)	2.071(1)	2.069(1)	2.072(1)	2.075(1)	2.075(1)	2.079(1)	2.092(1)	2.094(1)	2.103(1)
A-O2 (x2)	2.108(2)	2.111(2)	2.111(1)	2.114(1)	2.115(1)	2.116(1)	2.125(1)	2.123(1)	2.130(1)
A-O2 (x2)	2.152(1)	2.154(1)	2.155(1)	2.157(1)	2.157(1)	2.159(1)	2.158(1)	2.159(1)	2.162(1)
Average	2.110	2.111	2.112	2.115	2.115	2.116	2.118	2.125	2.132
V (Å <sup>3</sup> )	12.265	12.270	12.290	12.340	12.348	12.391	12.510	12.521	12.636
OQE	1.015	1.015	1.015	1.015	1.015	1.015	1.015	1.015	1.015
OAV	50.48	51.76	52.71	52.59	52.45	52.42	51.86	52.09	51.92
ELD	4.20	4.28	4.35	4.36	4.36	4.37	4.55	4.56	4.62
Ct(A)-A	0.222(1)	0.226(1)	0.228(1)	0.228(1)	0.227(1)	0.227(1)	0.224(1)	0.224(1)	0.223(1)
<b>Site B</b>									
B-O1	1.953(2)	1.952(1)	1.947(1)	1.945(1)	1.945(1)	1.942(1)	1.932(1)	1.929(1)	1.920(1)
B-O1	2.090(1)	2.089(1)	2.090(1)	2.089(1)	2.090(1)	2.089(1)	2.081(1)	2.080(1)	2.079(1)
B-O2	1.847(1)	1.841(1)	1.839(1)	1.834(1)	1.833(1)	1.830(1)	1.814(1)	1.813(1)	1.800(1)
B-O3	2.234(1)	2.237(1)	2.241(1)	2.247(1)	2.247(1)	2.251(1)	2.263(1)	2.265(1)	2.276(1)
B-O3	1.962(1)	1.958(1)	1.959(1)	1.957(1)	1.958(1)	1.958(1)	1.956(1)	1.954(1)	1.955(1)
B-O3	2.059(1)	2.061(1)	2.059(1)	2.062(1)	2.061(1)	2.062(1)	2.064(1)	2.064(1)	2.066(1)
Average	2.024	2.023	2.023	2.022	2.022	2.022	2.019	2.018	2.016
V (Å <sup>3</sup> )	10.694	10.668	10.652	10.644	10.642	10.633	10.560	10.542	10.504
OQE	1.026	1.027	1.028	1.028	1.028	1.029	1.030	1.031	1.032
OAV	78.05	79.31	81.16	82.23	82.38	83.18	87.58	88.42	91.79
ELD	3.31	3.34	3.36	3.33	3.33	3.35	3.39	3.39	3.38
Ct(B)-B	0.297(1)	0.301(1)	0.304(1)	0.308(1)	0.308(1)	0.310(1)	0.321(1)	0.322(1)	0.331(1)
<b>Interpolyhedral geometrical parameters</b>									
A-A	3.202(1)	3.205(1)	3.206(1)	3.207(1)	3.206(1)	3.207(1)	3.202(1)	3.202(1)	3.201(1)
B-B	3.249(1)	3.250(1)	3.253(1)	3.256(1)	3.256(1)	3.257(1)	3.262(1)	3.261(1)	3.267(1)
Ct(A)-Ct(A)	2.953	2.951	2.950	2.950	2.950	2.951	2.950	2.948	2.949
Ct(B)-Ct(B)	2.929	2.926	2.925	2.924	2.924	2.924	2.919	2.917	2.916
TILT A (°)	69.15	69.11	69.02	68.91	68.88	68.79	68.47	68.40	68.06
TILT B <sub>A</sub> (°)	76.15	76.32	76.36	76.47	76.52	76.61	77.08	77.08	77.32
TILT B <sub>B</sub> (°)	54.79	54.60	54.66	54.56	54.49	54.51	54.30	54.18	54.21

Notes: standard deviations are given in parentheses.

ELD (Edge Length Distortion) is defined as  $ELD = \frac{100}{n} \sum_{i=1}^n \frac{(X-X)_i - (X-X)_m}{(X-X)_m} \%$ , where  $m$  = average (Renner and Lehmann 1986). Ct(A) and Ct(B) are the centroids of polyhedra A and B, respectively.**TABLE 6B.** Bond distances (Å) and selected geometrical parameters for sample KRA n.4

$Q_m$	0.565	0.674	0.742	0.817	0.844	0.922	0.960	1.000	
<b>Site A</b>									
A-O1 (x2)	2.095(3)	2.091(3)	2.093(3)	2.108(3)	2.110(3)	2.119(3)	2.131(3)	2.138(3)	
A-O2 (x2)	2.123(3)	2.131(3)	2.127(3)	2.135(3)	2.137(3)	2.148(3)	2.154(3)	2.158(3)	
A-O2 (x2)	2.185(3)	2.201(3)	2.196(3)	2.204(3)	2.200(3)	2.207(3)	2.215(3)	2.217(3)	
Average	2.134	2.141	2.139	2.149	2.149	2.158	2.167	2.171	
V (Å <sup>3</sup> )	12.617	12.719	12.666	12.842	12.834	13.008	13.152	13.232	
OQE	1.019	1.020	1.020	1.021	1.021	1.021	1.021	1.021	
OAV	63.56	66.63	68.62	69.76	71.00	69.94	71.04	71.81	
ELD	4.75	4.69	4.85	5.10	5.05	5.08	5.19	5.25	
Ct(A)-A	0.251	0.262	0.263	0.265	0.266	0.265	0.267	0.267	
<b>Site B</b>									
B-O1	1.960(3)	1.957(3)	1.950(3)	1.941(3)	1.937(3)	1.936(3)	1.925(3)	1.921(3)	
B-O1	2.087(3)	2.093(3)	2.089(3)	2.084(3)	2.082(3)	2.076(3)	2.073(3)	2.069(3)	
B-O2	1.858(3)	1.838(3)	1.840(3)	1.828(3)	1.828(3)	1.816(3)	1.803(3)	1.800(3)	
B-O3	2.231(3)	2.247(3)	2.244(3)	2.256(3)	2.257(3)	2.267(3)	2.277(3)	2.282(3)	
B-O3	1.967(3)	1.956(3)	1.958(3)	1.959(3)	1.956(3)	1.955(3)	1.953(3)	1.957(3)	
B-O3	2.057(3)	2.061(3)	2.057(3)	2.056(3)	2.058(3)	2.063(3)	2.065(3)	2.064(3)	
Average	2.027	2.025	2.023	2.021	2.020	2.019	2.016	2.015	
V (Å <sup>3</sup> )	10.731	10.701	10.657	10.605	10.590	10.570	10.508	10.493	
OQE	1.026	1.027	1.028	1.029	1.029	1.030	1.032	1.032	
OAV	78.15	79.56	81.42	84.25	85.12	86.18	89.20	91.03	
ELD	3.60	3.37	3.50	3.55	3.50	3.53	3.54	3.59	
Ct(B)-B	0.292	0.302	0.303	0.309	0.311	0.316	0.323	0.326	
<b>Interpolyhedral geometrical parameters</b>									
A-A	3.258	3.267	3.266	3.271	3.271	3.274	3.277	3.279	
B-B	3.259	3.265	3.263	3.267	3.267	3.270	3.273	3.276	
Ct(A)-Ct(A)	2.973	2.968	2.965	2.967	2.966	2.969	2.969	2.970	
Ct(B)-Ct(B)	2.943	2.938	2.935	2.934	2.932	2.931	2.929	2.929	
TILT A (°)	68.53	68.17	68.17	67.77	67.72	67.40	67.04	66.92	
TILT B <sub>A</sub> (°)	77.51	77.60	77.70	78.22	78.33	78.83	79.18	79.36	
TILT B <sub>B</sub> (°)	53.22	52.77	52.70	52.63	52.42	52.02	51.69	51.77	

Notes: standard deviations are given in parentheses.

ELD (Edge Length Distortion) is defined as  $ELD = \frac{100}{n} \sum_{i=1}^n \frac{(X-X)_i - (X-X)_m}{(X-X)_m} \%$ , where  $m$  = average (Renner and Lehmann 1986). Ct(A) and Ct(B) are the centroids of polyhedra A and B, respectively.

ing faces of adjacent polyhedra (highlighted in Fig. 9). These angles will be referred to as TiltA (for the A chain), TiltB<sub>A</sub> (for the side of the B chain connected to the A chain), and TiltB<sub>B</sub> (for the side of the B chain connected to another B chain). In a chain of perfectly regular octahedra, these angles are 70.528°.

### Fe-Mn substitution

**Unit-cell parameters.** Substitution of Fe for the larger Mn cation across the solid solution causes a decrease of all unit-cell parameters. The variation of unit-cell volume with composition across the Fe-Mn join in *Pbcn* columbites may be described by:  $V(\text{cell}) = 421.77(26) - 9.53(49) \cdot X_{\text{Fe}}$ , Å<sup>3</sup> ( $R = 0.997$ ). As evident from Figure 2, the variations as a function of  $X_{\text{Fe}}$  of all the single unit-cell parameters are linear within the resolution of our measurements.

The linear trend agrees with the unit-cell parameters relations derived by Ercit et al. (1995). Unit-cell parameters calculated using the equation of Ercit et al. (1995) for samples of the same

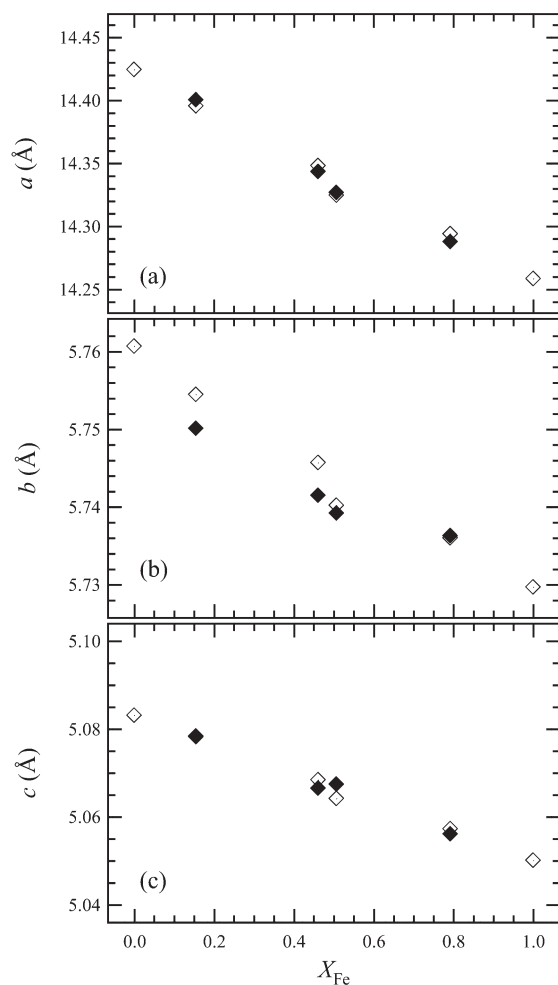


**FIGURE 2.** Variation of unit-cell parameters as a function of  $X_{\text{Fe}}$  for ordered columbite samples (solid diamonds) and expected values on the basis of regressions from Ercit et al. (1995) (open diamonds). End-members values are calculated from the equations in Ercit et al. (1995) for compositions  $\text{Mn}(\text{Ta}_{0.05}\text{Nb}_{0.95})_2\text{O}_6$  and  $\text{Fe}(\text{Ta}_{0.05}\text{Nb}_{0.95})_2\text{O}_6$ . (a)  $a$  vs.  $X_{\text{Fe}}$ , (b)  $b$  vs.  $X_{\text{Fe}}$ , (c)  $c$  vs.  $X_{\text{Fe}}$ .

composition as the ones of the present study as well as for  $\text{Fe}(\text{Ta}_{0.05}\text{Nb}_{0.95})_2\text{O}_6$  and  $\text{Mn}(\text{Ta}_{0.05}\text{Nb}_{0.95})_2\text{O}_6$  are reported in Figure 2 for comparison. There is good agreement between observed and calculated unit-cell parameters, although the  $b$  and  $c$  values for the Mn-rich samples are more scattered.

**A and B polyhedra.** The geometry (i.e., bond lengths and angles) of the B site within Fe-Mn columbites appears to be dependent only on the occupancy of the site itself, and not on the occupancy of neighboring sites. In Figure 3 the octahedral mean cation-O bond lengths for both the octahedral sites are shown. The mean A-O distance (Fig. 3a) decreases almost linearly as a function of iron content, as a consequence of a linear decrease of all individual bond lengths (Table 5). In contrast, the B-O distance (Fig. 3b) remains constant across the Fe-Mn join. The occupancy of the B site is in fact kept constant across the solid solution, as it is not directly involved in the cation substitution.

The two octahedral sites are both quite irregular and show different types of distortion (see data in Table 5). The A polyhedron presents a quite irregular external arrangement of the oxygen atoms, giving a high ELD value (higher than for the B site). On the other hand, the (Nb,Ta) octahedra show a relatively regular oxygen cage associated with a fairly large spread of individual bond-lengths. This is because of the displacement of the central metal atom from the geometrical centre of the polyhedron. Going from manganocolumbite to ferrocolumbite the A site is reduced in volume and becomes less distorted both with respect to its external shape and to the cation coordination sphere. The edge-length distortion parameter  $\text{ELD}_A$  decreases linearly as a function of Fe fraction (Fig. 4a). This may be attributed to the decreasing mismatch between A and B chains, due to a smaller difference in volume between A and B octahedra. The distance of the metal cation to the centroid of the octahedron  $\text{Ct}(A)-A$ ,

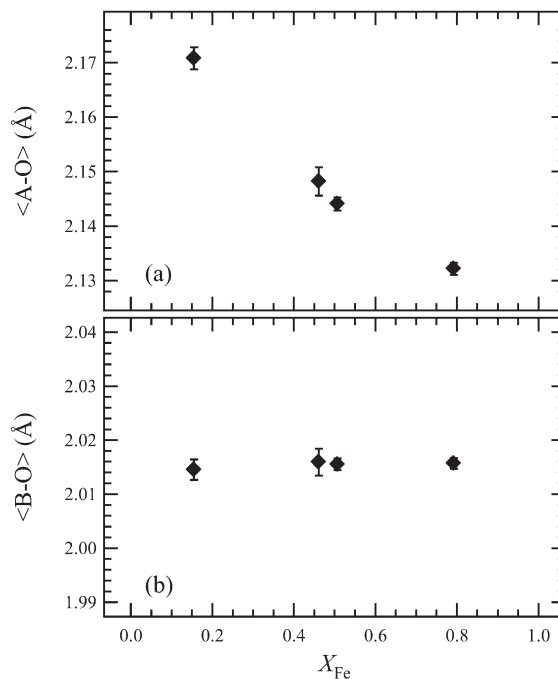


**FIGURE 3.** Mean cation-O bond distances as a function of  $X_{\text{Fe}}$ . (a)  $\langle A-O \rangle$  vs.  $X_{\text{Fe}}$ , (b)  $\langle B-O \rangle$  vs.  $X_{\text{Fe}}$ . Same symbols as for Figure 2.

reported in Figure 4b, decreases linearly with  $X_{\text{Fe}}$  as well. This effect is associated with a decrease along the octahedral chain of the cation-cation repulsion that is larger for the larger cation.

Fe-Mn exchange at the A site across the join does not affect the geometry of the B site; as is evident from the data in Table 5, the polyhedral volume remains constant and both the distortion parameters  $\text{ELD}_B$  and  $\text{Ct}(B)$ -B of all the samples studied across the solid solution show no significant differences.

**Chains.** As is evident from Figure 5, where the variations of  $\text{Tilt}_A$ ,  $\text{Tilt}_{B_A}$ , and  $\text{Tilt}_{B_B}$ , respectively, are reported as a function of  $X_{\text{Fe}}$ , the tilting angles of the B chain are farther from the ideal value than those of the A chain. Nevertheless, all three angles become closer to the ideal with substitution of Fe for Mn at the A site. In fact the  $\text{Tilt}_A$  angle increases linearly with increasing Fe content as does  $\text{Tilt}_{B_B}$ , which is the smallest and the most irregular angle. On the other hand, the  $\text{Tilt}_{B_A}$  angle decreases linearly, varying from  $79.4^\circ$  for the Mn-rich sample to  $77.4^\circ$  for the ferrocolumbite BRA.

### $M^{2+}$ - $M^{5+}$ ordering

**Unit-cell parameters.** Variations of lattice constants and cell volume as a function of  $Q_m$  for samples KRA n.4 and BRA n.18 are shown in Figure 6. In both cases, the  $a$  cell parameter increases while the  $c$  cell parameter decreases almost linearly with increasing degree of order. Slight deviations from linearity can be observed at low degrees of order. A non-linear behavior is shown by the  $b$  cell parameter that has a minimum at  $Q_m \sim 0.7$ . Unit-cell parameters obtained from various single crystals (either untreated or annealed) from sample KRA and characterized by a wider range of degrees of order are reported in the graph in order to more clearly confirm this trend.

**A and B polyhedra.** The mean octahedral A-O bond lengths

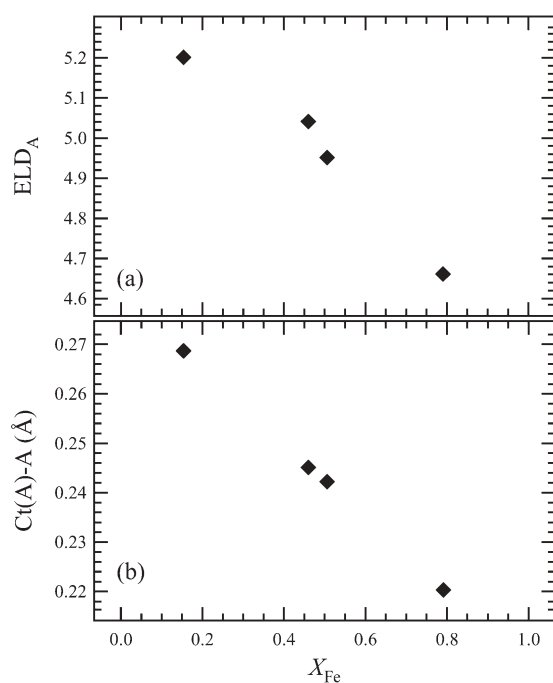


**FIGURE 4.** Distortion parameters of A site as a function of  $X_{\text{Fe}}$ . (a)  $\text{ELD}_A$  vs.  $X_{\text{Fe}}$ , (b)  $\text{Ct}(A)\text{-A}$  vs.  $X_{\text{Fe}}$ . Same symbols as for Figure 2.

for both the samples are shown in Figure 7a. They increase almost linearly as a function of  $Q_m$ , but with a change of slope at  $Q_m = 0.7$ . Site A is a quite irregular octahedron. The oxygen cage becomes more distorted with increasing  $Q_m$ , as indicated by the increase in the  $\text{ELD}_A$  parameter shown in Figure 7b. On the other hand, the metal cation moves only slightly from the centroid of the octahedron and its displacement does not vary significantly with increasing degree of order (see Tables 6a and 6b). It is worth noting that the A site is generally more distorted with respect to both edge and bond lengths in the Mn-rich sample at all degrees of order.

The B site is smaller than the A site and shows a very slight decrease of the average B-O bond length as a consequence of the presence of the small pentavalent cations (Fig. 8a). With respect to the A site, it shows a more regular external arrangement of oxygen atoms that seems not to be affected by the ordering process. In fact, as is evident from Tables 6a and 6b,  $\text{ELD}_B$  is always lower than  $\text{ELD}_A$ , and remains constant for all  $Q_m$  values. In contrast, distortion of the bond angles is quite large (see OAV in Tables 6a and 6b) because of the displacement of the B cation from the

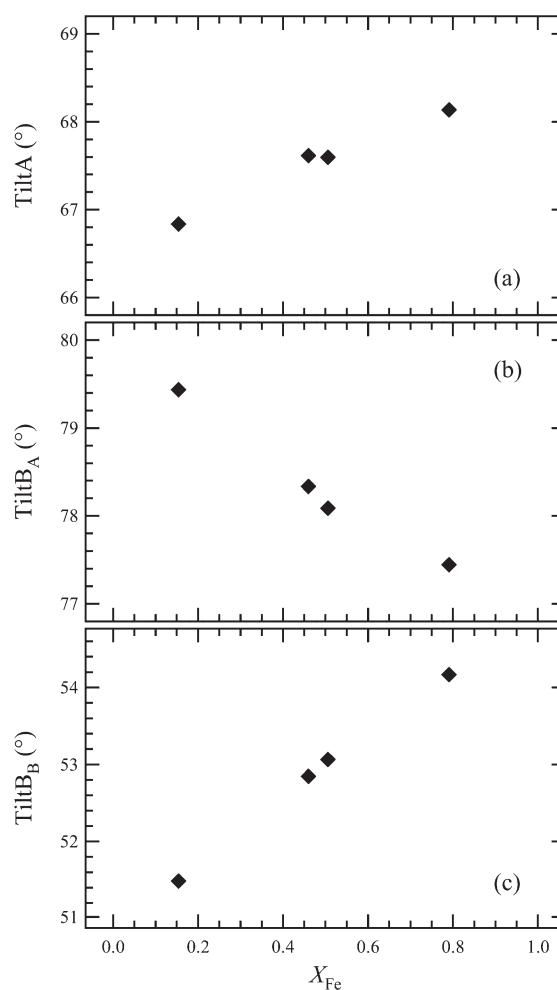


**FIGURE 5.** Variation of tilting angles of A and B chains as a function of  $X_{\text{Fe}}$ . (a)  $\text{Tilt}_A$  vs.  $X_{\text{Fe}}$ , (b)  $\text{Tilt}_{B_A}$  vs.  $X_{\text{Fe}}$ , (c)  $\text{Tilt}_{B_B}$  vs.  $X_{\text{Fe}}$ . Same symbols as for Figure 2.

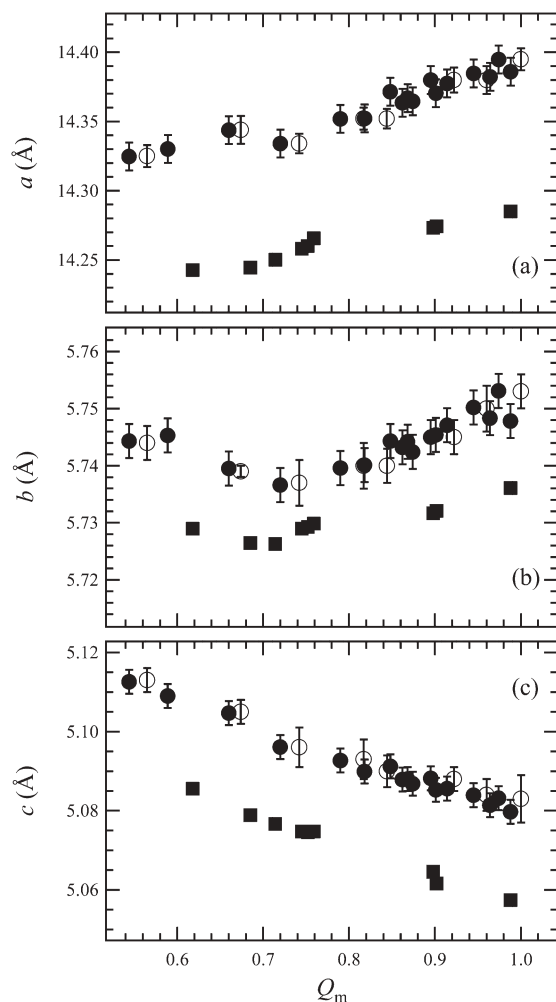


**FIGURE 6.** Variation of unit-cell parameters as a function of degree of order. (a)  $a$  vs.  $Q_m$ , (b)  $b$  vs.  $Q_m$ , (c)  $c$  vs.  $Q_m$ . Open circles: KRA n.4; solid squares: BRA n.18; solid circles: different crystals from sample KRA. For sample BRA, the vertical size of the symbols exceeds the uncertainties in unit-cell parameters.

centroid of the polyhedron. Such an offset, Ct(B)-B, increases sharply and linearly as a function of  $Q_m$  (Fig. 8b).

As Kunz and Brown (1995) pointed out, for the ordered columbite structure, octahedral distortion at the B site may be ascribed to at least two effects working symbiotically. Firstly, the occurrence of out-of-centre distortion of  $d^0$  transition metal cations can be understood in terms of the second-order Jahn-Teller (SOJT) effect. Secondly, octahedral chains share semi-adjacent edges, hence the cations are brought into contact and tend to relax by moving away from each other. To minimize the cation-cation repulsion along the octahedral chain, the B metal moves along the **b** crystallographic direction, as depicted in Figure 9. The shift of the B cation from the centroid of the octahedron with the entrance of the pentavalent cation into the site allows for compensation between both these effects. Coordination at the metal center becomes in fact more distorted, as imposed by the SOJT effect, and at the same time the B-B distance along the chain increases, as is evident from the data in Tables 6a and 6b.

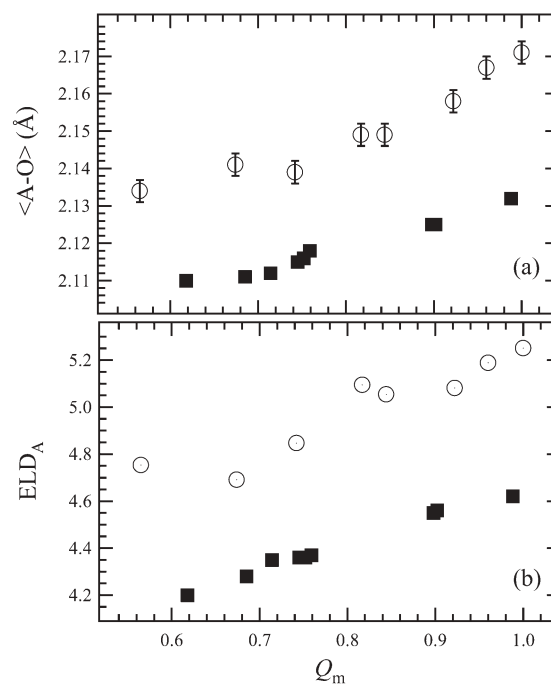


**FIGURE 7.** Variations of mean A-O bond distance (a) and edge length distortion  $ELD_A$  (b) as a function of  $Q_m$ . Same symbols as for Figure 6. For sample BRA, the vertical size of the symbols exceeds the uncertainties in  $\langle A-O \rangle$  bond distance.

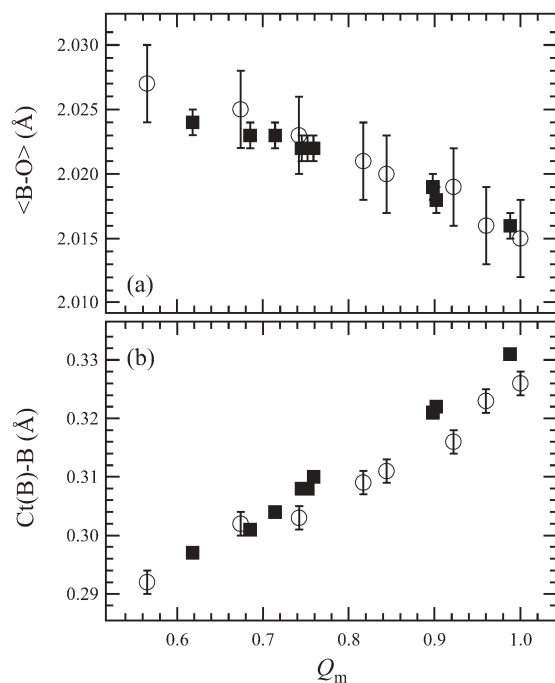


**FIGURE 8.** Variations of mean B-O bond distance (a) and Ct(B)-B distance (b) as a function of  $Q_m$ . Same symbols as for Figure 6. For sample BRA, the vertical size of the symbols exceeds the uncertainties in Ct(B)-B distance.

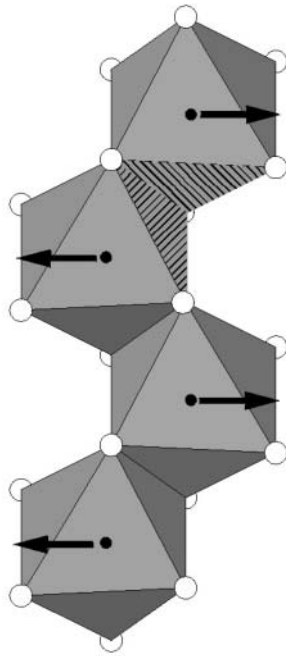


**FIGURE 9.** Schematic representation of chains of edge-sharing octahedra. The arrows indicate the direction of cation displacement arising from cation-cation repulsion at the B site. Two edge-sharing faces that form the Tilt angles (see text) are highlighted in the figure.

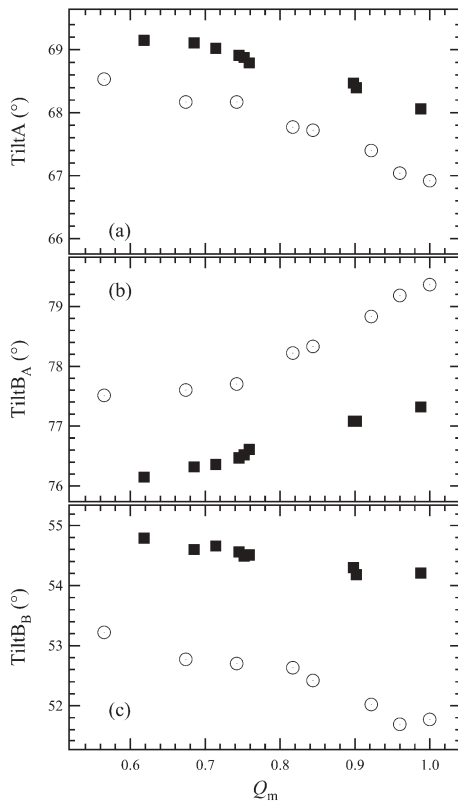


**FIGURE 10.** Variation of tilting angles as a function of degree of order. (a) TiltA vs.  $Q_m$ , (b) TiltB<sub>A</sub> vs.  $Q_m$ , (c) TiltB<sub>B</sub> vs.  $Q_m$ . Same symbols as for Figure 6.

It is also worth noting that the values of all geometrical parameters associated with the B site are almost identical for the two samples at all  $Q_m$ . This further confirms that the geometry of the site is controlled by the pentavalent cations and appears not to be influenced by the occupancy of the neighboring A sites.

**Chains.** As shown in Figure 10a, the angle TiltA, for both samples KRA and BRA, decreases slightly with increasing  $Q_m$ . The A chain is more folded for the KRA sample as the A polyhedron is larger when occupied by the larger Mn ion. In contrast, the angle TiltB<sub>A</sub> (Fig. 10b) increases with increasing

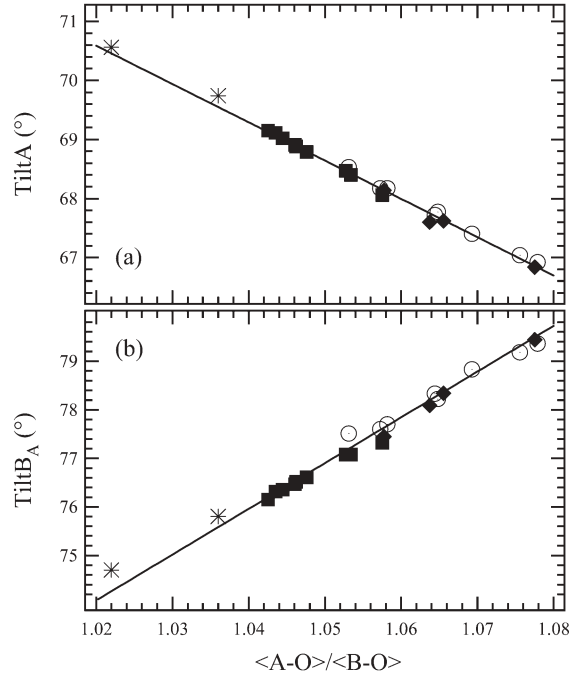


**FIGURE 11.** Variation of tilting angles of A and B chains as a function of the mismatch between A and B layers. (a) TiltA vs.  $\langle A-O \rangle / \langle B-O \rangle$ , (b) TiltB<sub>A</sub> vs.  $\langle A-O \rangle / \langle B-O \rangle$ . Solid diamonds: ordered columbite samples; open circles: KRA n.4; solid squares: BRA n.18; stars: data from Wenger et al. (1991); solid line: linear regression through the samples of this study.

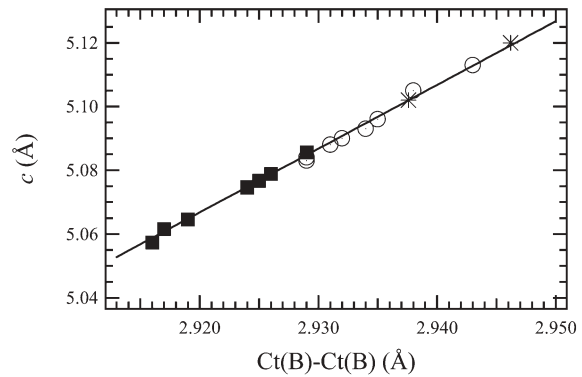


**FIGURE 12.** Variation of the  $c$  cell parameter as a function of the distance between centroids of two adjacent B sites. Same symbols as for Figure 11.

$Q_m$ , to accommodate the enlargement of the A site that is being occupied by the larger divalent cations.  $TiltB_A$  is larger for the Mn-rich sample as well. The angle  $TiltB_B$  shows an opposite trend as shown in Figure 10c.

### Cation exchange: interpolyhedral compensations

Interpolyhedral connections compensate for mismatch between the volumes of sites. The tilting angles approach the ideal value for regular octahedral chains with decreasing mismatch between A and B layers. Staggering of the chains seems to be entirely dependent upon the volumes of the A and B polyhedra, irrespective of the nature of the cations occupying them. As evident from Figures 11a and 11b, the tilting angles relative to both the A and B chains,  $TiltA$  and  $TiltB_A$ , for all the samples converge on the same line when plotted against the ratio  $\langle A-O \rangle / \langle B-O \rangle$ . For a further confirmation of this trend, geometrical parameters obtained from data by Wenger et al. (1991) on partially disordered natural samples were compared with those of the present study. As evident from figures, they fall on the same line although these samples show different chemical composition and degree of order.

The contraction of volume of the B polyhedron together with the folding of the chain cause the distance between the centroids of two adjacent polyhedra along the B chain to decrease sharply and almost linearly with increasing  $Q_m$  [see  $Ct(B)-Ct(B)$  in Tables 6a and 6b for samples BRA and KRA, respectively]. As is evident from Figure 12, where the relationship between these two parameters for the samples of this study and for samples taken from the literature (Wenger et al. 1991) are reported, this distance fixes the  $c$  cell parameter of the columbite structure.

### ACKNOWLEDGMENTS

The authors thank C. Cipriani and G. Mazzetti (University of Florence) for providing the samples and S. Bigi for the microprobe analyses. Funding by the Department of Earth Sciences of the University of Modena is also acknowledged. M.A. Carpenter is thanked for helpful discussions. Comments by two anonymous reviewers helped to improve the manuscript. Financial support was provided by the Italian MIUR project "Mineral physics and technological applications of columbite-tantalite-tapiolite system."

### REFERENCES CITED

- Augsburger, M.S., Pedregosa, J.C., Sosa, G.M., and Mercader, R.C. (1999) Mössbauer assessment of cation disorder in columbite-tantalite minerals. *Journal of Solid State Chemistry*, 143, 219–223.
- Betteridge, P.W., Carruthers, J.R., Cooper, R.I., Prout, K., and Watkin, D.J. (2003) *CRYSTALS* version 12: software for guided crystal structure analysis. *Journal of Applied Crystallography*, 36, 1487.
- Blessing, R.H. (1995) An empirical correction for absorption anisotropy. *Acta Crystallographica*, A51, 33–38.
- Blessing, R.H., Coppens, P., and Becker, P. (1974) Computer analysis of step-scanned X-ray data. *Journal of Applied Crystallography*, 7, 488–492.
- Cannillo, E., Germani, G., and Mazzi, F. (1983) New crystallographic software for Philips PW 1100 single crystal diffractometer. CNR Centro di Studio per la Cristallografia, Internal Report 2.
- Carruthers, J.R. and Watkin, D.J. (1979) Chebyshev weighting. *Acta Crystallographica*, A35, 698–699.
- Černý, P. and Turnock, A.C. (1971) Niobium-tantalum minerals from granitic pegmatites at Greer Lake, southeastern Manitoba. *Canadian Mineralogist*, 10, 755–772.
- Černý, P., Goad, B.E., Hawthorne, F.C., and Chapman, R. (1986) Fractionation trends of the Nb- and Ta-bearing oxide minerals in the Greer Lake pegmatitic granite and its pegmatite aureole, southwestern Manitoba. *American Mineralogist*, 71, 501–517.
- Donovan, J.J. and Rivers, M.L. (1990) PRSUPR—A PC based automation and analysis software package for wavelength-dispersive electron-beam microanalysis. *Microbeam Analysis*, 66–68.
- Ercit, T.S., Wise, M.A., and Černý, P. (1995) Compositional and structural systematics of the columbite group. *American Mineralogist*, 80, 613–619.
- Giese, R.F. Jr. (1975) Electrostatic energy of columbite/ixiolite. *Nature*, 256, 31–32.
- Grice, J.D., Ferguson, R.B., and Hawthorne, F.C. (1976) The crystal structure of tantalite, ixiolite and wodginitite from Bernic Lake, Manitoba. I. Tantalite and ixiolite. *Canadian Mineralogist*, 14, 550–560.
- Ibers, J.A. and Hamilton, W.C. (1974) *International Tables for X-ray Crystallography*, 4, p. 99–101. Kynoch Press, Birmingham, U.K.
- Komkov, A.I. (1970) Relationship between the X-ray constants of columbites and composition. *Doklady Akademii Nauk SSSR*, 195, 117–119.
- Kunz, M. and Brown, D. (1995) Out-of-center distortions around octahedrally coordinated  $d^0$  transition metals. *Journal of Solid State Chemistry*, 115, 395–406.
- Larson, A.C. (1970) The inclusion of secondary extinction in least-squares refinement of crystal structures. In F.R. Ahmed, S.R. Hall, and C.P. Huber, Eds., *Crystallographic Computing*, 291–294. Munksgaard, Copenhagen.
- Lehman, M.S. and Larsen, F.K. (1974) A method for location of the peaks in step-scanned measured Bragg reflections. *Acta Crystallographica*, A30, 580–584.
- Nickel, E.H., Rowland, J.F., and McAdam, R.C. (1963) Ixiolite—A columbite substructure. *American Mineralogist*, 48, 961–979.
- North, A.C.T., Phillips, D.C., and Mathews, F.S. (1968) A semi-empirical method of absorption correction. *Acta Crystallographica*, A24, 351–359.
- Renner, B. and Lehmann, G. (1986) Correlation of angular and bond length distortion in  $TO_4$  units in crystals. *Zeitschrift für Kristallographie*, 175, 43–59.
- Robinson, K., Gibbs, G.V., and Ribbe, P.H. (1971) Quadratic elongation, a quantitative measure of distortion in co-ordination polyhedra. *Science*, 172, 567–570.
- Shannon, R.D. (1976) Revised effective ionic radii and systematic studies of interatomic distances in halides and chalcogenides. *Acta Crystallographica*, A32, 751–767.
- Turnock, A.C. (1966) Synthetic wodginitite, tapiolite and tantalite. *Canadian Mineralogist*, 8, 461–470.
- Weitzel, H. (1976) Kristallstrukturverfeinerung von Wolframiten und Columbiten. *Zeitschrift für Kristallographie*, 144, 238–258.
- Wenger, M., Armbruster, T., and Geiger, C.A. (1991) Cation distribution in partially ordered columbite from the Kings Mountain pegmatite, North Carolina. *American Mineralogist*, 76, 1897–1904.
- Wise, M.A., Turnock, A.C., and Černý, P. (1985) Improved unit-cell dimensions for ordered columbite-tantalite end members. *Neues Jahrbuch Für Mineralogie-Abhandlungen*, 8, 372–378.

MANUSCRIPT RECEIVED MARCH 10, 2004  
 MANUSCRIPT ACCEPTED DECEMBER 18, 2004  
 MANUSCRIPT HANDLED BY MARIA FRANCA BRIGATTI